

# The impact of faults and fluid flow on seismic images of a relay ramp over production time

Charlotte Botter<sup>1\*</sup>, Nestor Cardozo<sup>1</sup>, Isabelle Lecomte<sup>2,3</sup>, Atle Rotevatn<sup>4</sup> & Gaynor Paton<sup>5</sup>

<sup>1</sup> Department of Petroleum Engineering, University of Stavanger, 4036 Stavanger, Norway

<sup>2</sup> NORSAR, Gunnar Randers vei 15, 2007 Kjeller, Norway

<sup>3</sup> Present address: University of Bergen, Realfagbygget, Allègt. 41, Postboks 7803, 5020 Bergen, Norway

<sup>4</sup> Department of Earth Science, University of Bergen, 5020 Bergen, Norway

<sup>5</sup> GeoTeric, Trafalgar Street, Newcastle upon Tyne NE1 2LA, UK

\* Correspondence: [charlotte.botter@gmail.com](mailto:charlotte.botter@gmail.com)

**Abstract:** Relay ramps can act as conduits for fluid flow in producing hydrocarbon reservoirs, but the two bounding faults are often at the limit of seismic resolution. To study the impact of relay ramps and their fluid composition on seismic data, we present an integrated workflow combining flow simulation in a geomodel of an outcrop relay ramp, forward seismic modelling and seismic-attribute-based volume extraction. In the chosen outcrop of the Arches National Park (Utah, USA), the petrophysical properties are conditioned by deformation bands present in the sandstone, and are used to run a simple water injector–oil producer fluid-flow simulation. Pre-stack depth-migration seismic images are obtained at  $t=0$ ,  $t_1=10$  and  $t_2=20$  years of the flow simulation. The seismic image porosity changes at  $t=0$  when the model is oil-saturated, whereas the water–oil contacts have stronger amplitude contrasts at later stages. With an adapted attribute-based workflow, we are able to extract geobodies corresponding to the faults and the relay ramp from the three seismic cubes. By varying workflow parameters, we also show reservoir and acquisition conditions that can affect the resolution of the relay ramp on the seismic image either positively or negatively.

**Received** 9 February 2016; **revised** 27 September 2016; **accepted** 7 October 2016

Soft-linked relay ramps are zones between two fault segments that overlap along strike but are not yet linked (e.g. Peacock & Sanderson 1994; Childs *et al.* 1995; Walsh *et al.* 2003; Long & Imber 2010, 2012; Giba *et al.* 2012; Fossen & Rotevatn 2016). While faults can enhance or restrict fluid flow in hydrocarbon reservoirs, soft-linked relay zones can act as conduits for fluid flow regardless of the sealing capacities of the bounding faults (Hesthammer & Fossen 1997; Rotevatn *et al.* 2007, 2009; Manzocchi *et al.* 2010; Fachri *et al.* 2013). Faults are often 3D zones associated with the surrounding damage areas that are related to fault initiation, propagation, interaction and growth. These damage zones can be found in relay zones (e.g. Kim *et al.* 2004). In highly porous sandstone reservoirs, for example, the ramp damage zones can be composed of mesoscopic structures such as deformation bands, which are millimeter- to centimeter-thick zones of localized compaction, formed by disaggregation or cataclasis (e.g. Antonellini & Aydin 1994; Fossen *et al.* 2007). Cataclastic deformation bands are usually associated with a reduction in porosity, permeability and fluid flow (Antonellini & Aydin 1994; Rotevatn *et al.* 2007, 2009). Therefore, obtaining a good representation of the relay ramp and its damage zone during subsurface exploration is essential when accurately planning the reservoir production phase.

Seismic data are one of the main methods of investigating the subsurface. Faults and their damage zones are, however, difficult to image on seismic data because they are often at the limit of seismic resolution (e.g. Dutzer *et al.* 2010; Long & Imber 2010). Figure 1 shows the seismic expression of two laterally overlapping faults in a dip section (Fig. 1a) and on a time slice (Fig. 1b). The two faults are well imaged and the relay zone is discernible. However, depending on seismic resolution, the space between the relay-bounding faults and the magnitude of fault displacement, it may be difficult to image

the faults as two independent structures. Long & Imber (2010, 2012) used a dip-distortion attribute to map the deformation around linking faults and the architecture of the relay ramps on post-stack seismic data. Additional seismic-attribute-based methods have also been applied to map fault damage (Dutzer *et al.* 2010; Iacopini & Butler 2011; Iacopini *et al.* 2012, 2016; Botter *et al.* 2016; Torabi *et al.* 2016a, b). These studies highlight the potential of seismic data for characterizing fault damage and fault linkage. Deformation bands are sub-seismic features that cannot be directly imaged or interpreted on seismic profiles. However, they can be organized into clusters (e.g. Fossen *et al.* 2007) and, because they affect petrophysical properties and, therefore, fluid flow, they can impact the seismic response, especially during production (Fossen & Bale 2007). The presence of deformation bands can cause complex changes to seismic images over production time. Improving seismic characterization of relay ramps in highly porous sandstone reservoirs requires close attention to deformation band geometries, petrophysical properties and the associated subseismic-scale response.

During production, several properties within the relay ramp can have an additional influence on seismic data acquired at different stages, such as fluid saturation and pressure evolution. The movement of fluid contacts can be visible on 4D seismic imaging by comparing seismic data before production to data during or at the end of production. Therefore, when 4D seismic imaging is available, studying fluid displacement in the relay ramp over time can further constrain the interpretation of the relay ramp and its internal structure.

This paper investigates these issues and aims to:

- Understand the seismic response and improve the interpretation of relay ramps and the associated damage zones.

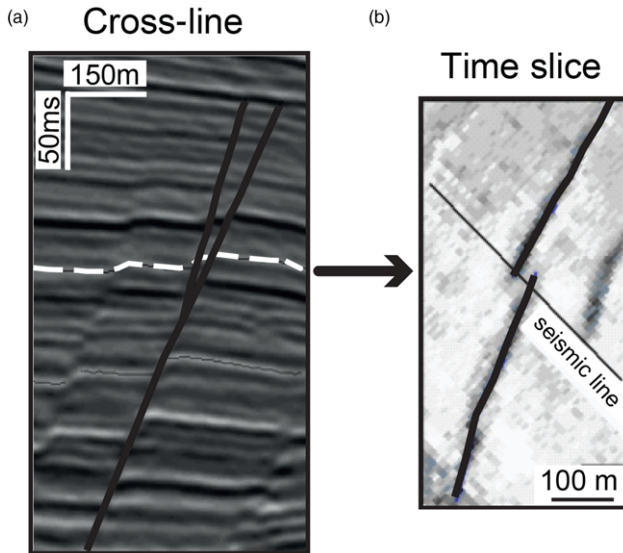


**Fig. 1.** Example of a relay ramp on seismic data. (a) Seismic cross-line showing two fault segments (black lines) at shallow depth, connecting at higher depth and offsetting the reflector (dashed white). (b) Time slice showing the two overlapping faults with a relay ramp between them. Modified from Walsh *et al.* (2003).

- Fine-tune seismic acquisition and processing parameters for the specific seismic characterization of relay ramps.
- Study fluid evolution within relay ramps on seismic images over a production period.
- Improve seismic interpretation of relay ramps, fault-related deformation and fluid contacts at reservoir depths and under production conditions.

We introduce an integrated workflow combining fluid-flow simulation in a geomodel of an outcrop relay ramp, forward seismic modelling at several stages of the flow simulation, and seismic-attribute-based interpretation (Fig. 2). Using an outcrop model of a relay ramp gives us control of the input structure, rock properties and subseismic features that influence fluid flow. The workflow differs to that of Botter *et al.* (2016), in that, instead of using mechanical fault models as the input, we produce seismic images using a geocellular reservoir model of a relay ramp outcrop model at different times during simulated water injection and oil production. This workflow allows us to modify the geological settings, such as reservoir properties, burial depth and overburden, as well as the fluid phase and seismic acquisition conditions.

The chosen outcrop analogue is the Delicate Arch Ramp, a well-exposed relay ramp in the middle Jurassic Entrada sandstone of the Arches National Park, Utah, USA (Rotevatn *et al.* 2007). The high-porosity sandstone of the outcrop and its estimated burial depth of

2 km make it an appropriate analogue to a clastic, highly porous and relatively clean sandstone reservoir. The relay ramp is characterized by a damage zone of cataclastic deformation bands. In the geocellular model, rock properties correspond to a homogeneous and high-porosity sandstone, and changes to these properties in the damage zone are conditioned by the density of deformation bands mapped in the outcrop (Rotevatn *et al.* 2007, 2009; Rotevatn & Fossen 2011) (Fig. 2a). The impact of several deformation-band frequencies and permeabilities on the fluid flow has been the topic of several publications (Rotevatn *et al.* 2009; Rotevatn & Fossen 2011; Fachri *et al.* 2013). In this study, we assume a simple fluid-flow simulation scenario, similar to that of Rotevatn *et al.* (2009) (Fig. 2b), and a forward seismic model at  $t = 0$ ,  $t_1 = 10$  and  $t_2 = 20$  years of the flow simulation, using a ray-based pre-stack depth-migration (PSDM) simulator (Lecomte 2008; Lecomte *et al.* 2015, 2016) (Fig. 2c). The seismic images of the reservoir at the three stages of the flow simulation provide insight into the seismic response of the relay ramp and its internal structure, as well as of the fluids moving through the ramp. An attribute-based seismic interpretation workflow is then applied to the seismic cubes to extract the volume corresponding to the relay structure and the fluid bodies (Fig. 2d). The combination of geology, geophysics and reservoir modelling allows us to visualize and evaluate the impact of relay ramp structures and moving fluid contacts on 4D seismic results.

## Context of the present study

This paper uses earlier research (i.e. reservoir modelling and fluid-flow simulations of the Delicate Arch Ramp outcrop (Utah) by Rotevatn *et al.* 2007, 2009) to explore seismic imaging and interpretation workflow. This section summarizes the settings, methods and results of these two studies (Rotevatn *et al.* 2007, 2009). Complete descriptions and additional information are available in these two publications.

## Structural setting

The Delicate Arch Ramp (Rotevatn *et al.* 2007) is located in the Arches National Park, Utah (USA) (Fig. 3a). The relay ramp is 150–200 m wide, and is defined by two normal, south-dipping, overlapping faults (Fig. 3b) in the middle Jurassic Entrada sandstone, an aeolian sandstone unit of interbedded dune and interdune deposits (Doelling 2001; Rotevatn *et al.* 2007).

Mesoscopic structures within the relay ramp consist of cataclastic deformation bands. These deformation bands are, on average, 2 mm wide, metres to tens of metres long and continuous in the vertical section. Based on detailed scan-line mapping of the relay ramp, Rotevatn *et al.* (2007) produced a map of the density of deformation bands (Fig. 3b). The frequency of the deformation bands is higher

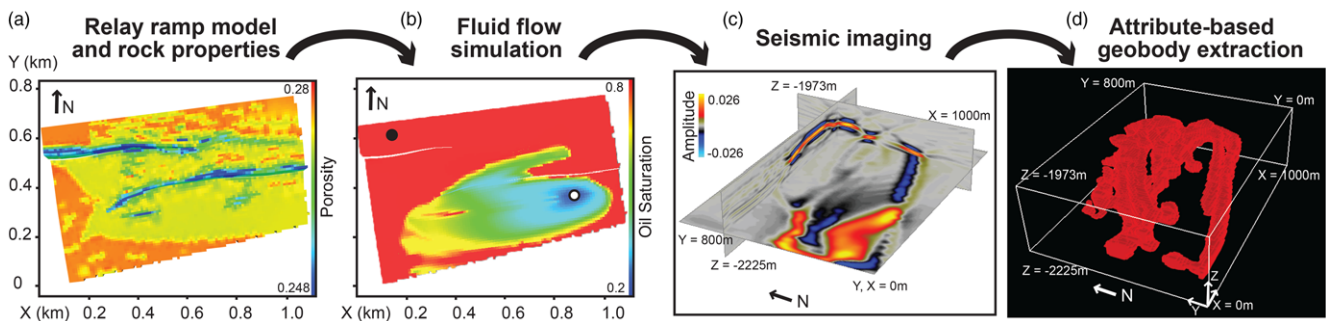


**Fig. 2.** Workflow of this study: (a) geomodel of the relay ramp and rock properties; (b) fluid-flow simulation; (c) PSDM simulated seismic cubes; and (d) attribute-based geobody extraction.

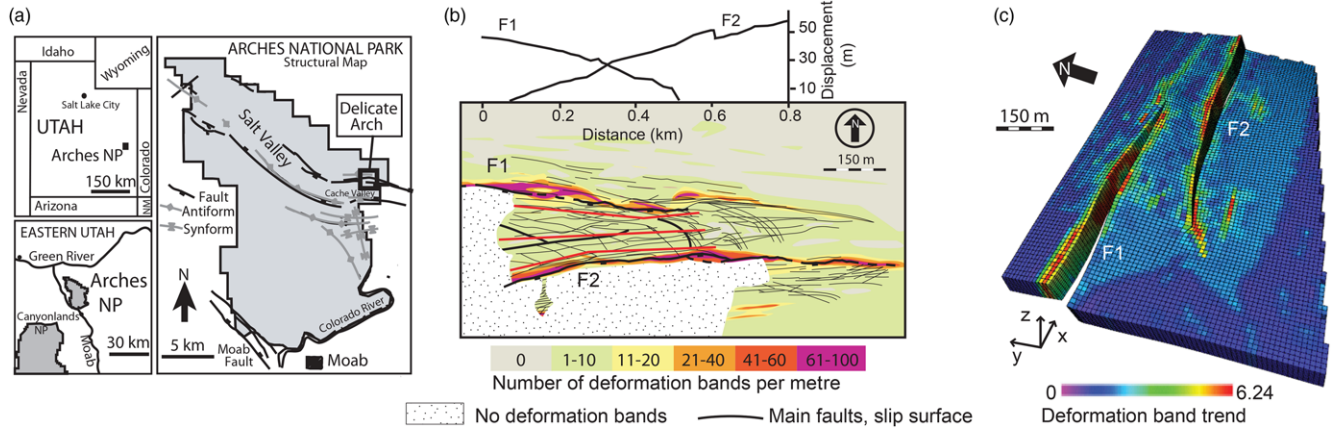


**Fig. 3.** Delicate Arch relay ramp. (a) Location. (b) Map of deformation-band frequency, with a fault displacement v. distance diagram in the upper part. (c) 3D view of geocellular model with deformation bands trend. (a) and (b) are modified from Rotevatn *et al.* (2007, 2009).

near the faults, but also ahead of the fault tiplines (e.g. east of the northern fault tipline: Fig. 3b).

### Geomodel

The information in Figure 3b was aggregated into a geomodel by converting the average number of deformation bands per metre of the six frequency classes (Fig. 3b) into a continuous deformation-band trend (Fig. 3c) (Rotevatn *et al.* 2009). The thickness of the geomodel was 50 m, and the size of the cells was ( $x$ – $y$ – $z$ )  $10 \times 10 \times 5$  m (Fig. 3c). Vertically, the deformation-band frequency was constant for the entire thickness of the reservoir (this is supported by field observations: Rotevatn *et al.* 2007).

### Rock properties

Antonellini & Aydin (1994, 1995) established the Entrada sandstone properties used in this study from both outcrop and laboratory measurements. The sandstone has a porosity of 28%, a horizontal permeability of 1000 mD and a vertical permeability of 100 mD. These values define the host-rock properties used in the reservoir model.

Based on the frequency of deformation bands within each cell of the geomodel (Fig. 3c), the sandstone properties can be modified due to faulting. Antonellini & Aydin (1994) showed that the permeability in the centre of a cataclastic deformation band is as low as 1 mD. Rotevatn *et al.* (2009) computed permeability in the geomodel in order to run fluid-flow simulations for several deformation-band frequencies and permeabilities, but kept the porosity constant throughout the model. They took into account the frequency and orientation of the deformation bands in each cell to compute the effective permeability. The vertical permeability of the sandstone was not modified as the deformation bands were subvertical and were assumed to not affect the vertical fluid flow. To compute effective permeability, Rotevatn *et al.* (2009) used a harmonic average of the rock mass for flow perpendicular to permeability barriers (i.e. along the  $y$  north direction), and an arithmetic average for flow parallel to the permeability barriers (along the  $x$  east direction) (Fig. 3c).

### Additional methodology

Our workflow explores the impact of relay ramps and the fluid flow across them on seismic images. Seismic reflectivity is directly related to bulk density and seismic velocities, and these two variables are dependent on the fluid content in the pore space. In addition to permeability, we therefore modified the porosity in the geomodel.

We ran the flow simulation using a new porosity trend corresponding to the median case of the deformation-band frequencies of Rotevatn *et al.* (2009). Our flow-simulation results differ from those of Rotevatn *et al.* (2009), although the set-up of the models was similar.

### Impact of deformation bands on porosity

Antonellini & Aydin (1994) showed that the initial porosity of 28% of the Entrada sandstone could be reduced to 1% in the centre of a cataclastic deformation band. In order to estimate the impact of deformation bands on porosity, we computed the porosity in each cell ( $\phi_{\text{cell}}$ ) using an arithmetic average based on the volume of deformation bands per cell and the remaining volume of the host sandstone:

$$\phi_{\text{cell}} = \frac{V_{\text{ss}}\phi_{\text{ss}} + V_{\text{DB}}\phi_{\text{DB}}}{V_{\text{total}}} \quad (1)$$

where  $V_{\text{ss}}$  is the volume of sandstone,  $\phi_{\text{ss}}$  is the initial porosity of the sandstone (0.28),  $V_{\text{DB}}$  is the volume of deformation bands,  $\phi_{\text{DB}}$  is the porosity of deformation bands (0.01) and  $V_{\text{total}}$  is the volume of the cell. As we do not distinguish the total porosity from the effective porosity, and as porosity is a scalar, this arithmetic average gives a good estimation of the porosity changes.

### Fluid-flow simulation

We use the computed porosity and permeability to simulate fluid flow in the relay ramp for one particular production case with the parameter values as described in Table 1. Similarly to Rotevatn *et al.* (2009), we used one water injector well located in the lower part of the relay ramp (i.e. the hanging wall of the southern fault) and one oil producer well in the upper part of the relay ramp (i.e. the

**Table 1.** Flow-simulation dynamic properties

Parameters	Values
Oil density	800 kg m <sup>-3</sup>
Water density	1100 kg m <sup>-3</sup>
Flow rates	
Injector	500 Sm <sup>3</sup> /day
Producer	500 Sm <sup>3</sup> /day
Bottom-hole pressure	
Injector	220 bar
Length of run until water breakout	
Base case	20 years
Low-porosity and low-permeability case	55 years



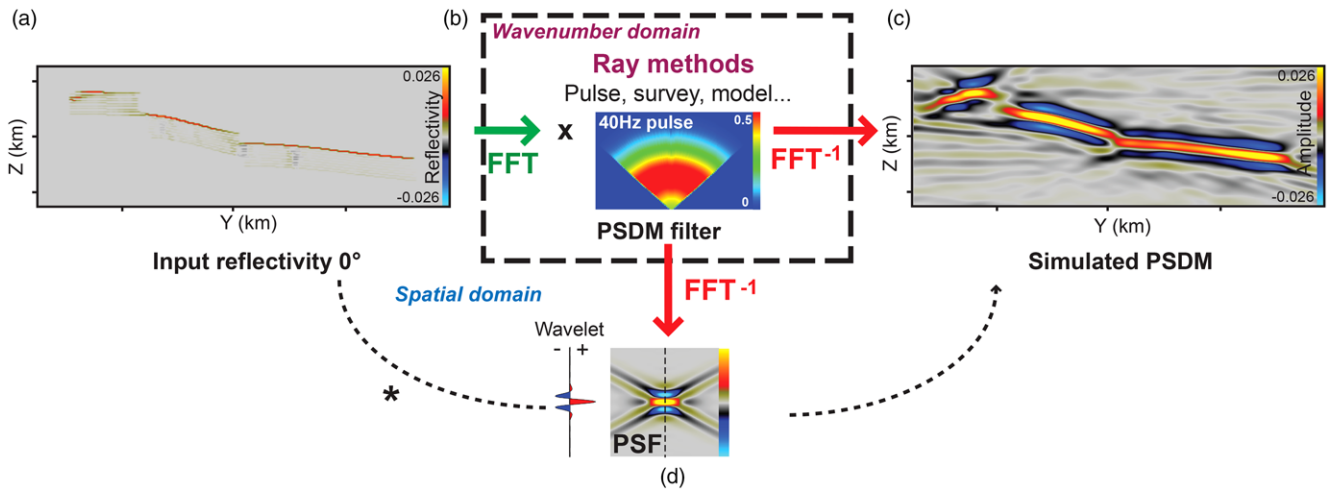


**Fig. 4.** PSDM simulator. (a) A reflectivity grid is input into the spatial domain. This input reflectivity is converted to the wavenumber domain using a FFT. (b) Ray methods are used to calculate a PSDM filter in the wavenumber domain. (c) The product of the PSDM filter and the input reflectivity in the wavenumber domain, plus an inverse FFT (FFT<sup>-1</sup>) on the result of this operation produces the simulated PSDM image. (d) The entire process is equivalent to the convolution of PSF corresponding to the PSDM filter in the spatial domain with the input reflectivity. The wavelet with its polarity is included next to the PSF.

footwall of the northern fault). Starting with an 80% oil-saturated reservoir, we observed oil displacement by water until water breakout occurred in the producer well. From the fluid-flow simulation, we obtained several models over time with different water saturations, which were subsequently used to simulate a 4D seismic image.

### Computation of elastic properties

The definition of elastic parameters – that is, P- and S-wave seismic velocities ( $V_P$ ,  $V_S$ ) and density  $\rho$  – is necessary to obtain the reflectivity for seismic modelling. To compute these parameters, we needed to take into account the porosity, the oil and water saturations, and their evolution during production time. The Gassmann theory (Gassmann 1951) is recognized as a reasonable model for high-porosity sandstone reservoirs (Mavko *et al.* 2009). To use Gassmann equations in our model, we considered the sandstone layer to be homogeneous and isotropic, and the pore space to be connected. Thus, the deformation bands were taken into

account only by their impact on the reservoir porosity and permeability. The Gassmann equation uses the porosity of the rock, and the bulk and shear moduli of the rock and fluids in place. We used standard values for the bulk and shear moduli for sandstone, brine water and oil. Combined with the porosity and water saturation, we were able to compute  $V_P$ ,  $V_S$  and  $\rho$  for the several stages of the fluid-flow simulation by applying the fluid-substitution technique and mixture model (Mavko *et al.* 2009).

### Simulation of seismic imaging

Seismic modelling is used to assess the impact of relay ramp structure and fluid contacts on seismic images. We used a ray-based 3D PSDM simulator (Lecomte 2008), which is a fast, practical and accurate tool for synthetic seismic imaging of geological models under a large range of geological and seismic acquisition settings (Lecomte *et al.* 2015, 2016). This simulator handles properly diffracted energy, such as that resulting from faults or other discontinuities. It also deals with 3D effects in resolution and

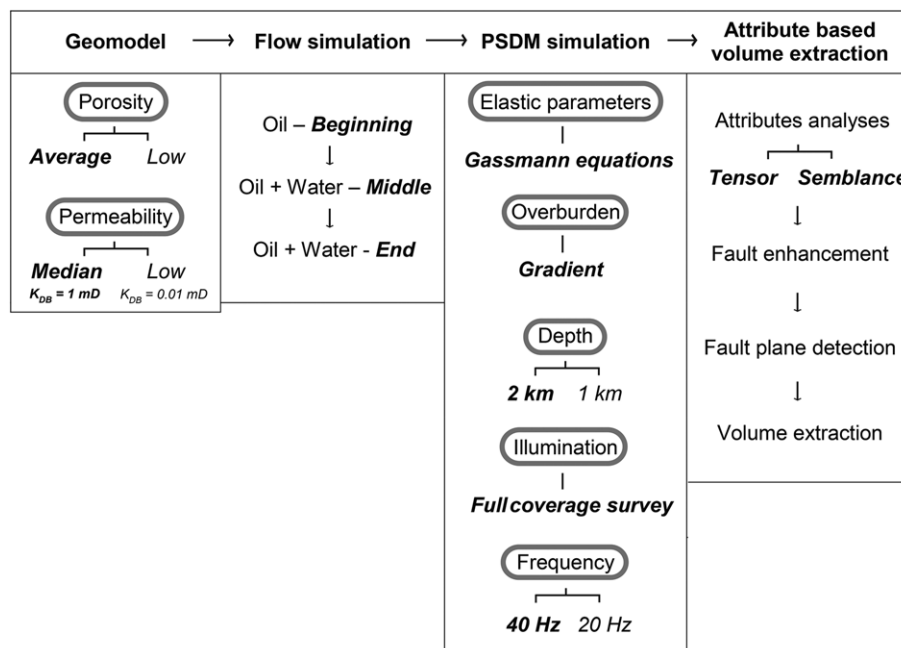


**Fig. 5.** Workflow and model parameters. The first row presents the four main steps of the workflow. The first column shows the main parameters needed to define the geomodel (grey outline). The second column presents the stages of the flow simulation. These three stages are used in the next steps. The third column describes the main parameters needed to run the PSDM simulator (grey outline). The last column presents the steps of the volume extraction. In all columns, bold corresponds to the base case and italics to the parameters that are varied.

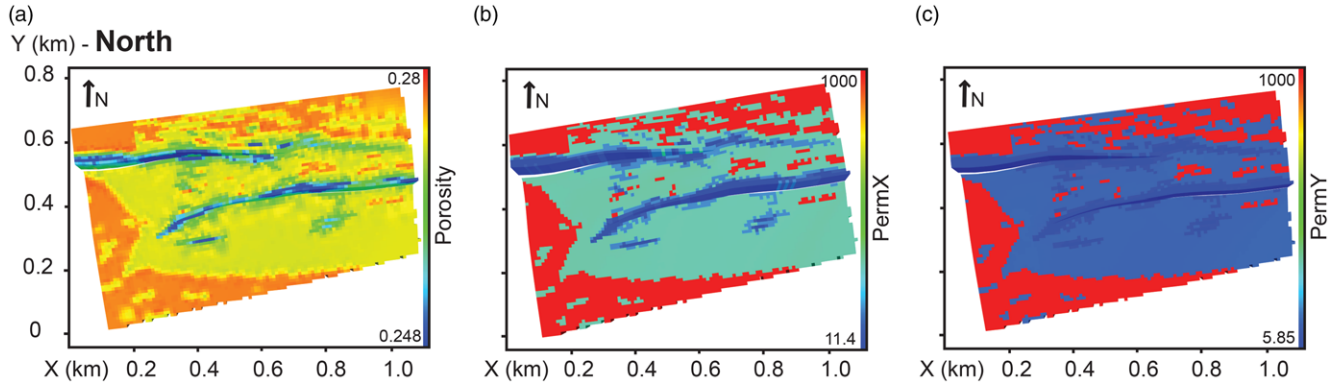


**Fig. 6.** Top view of rock properties of the Delicate Arch Ramp geomodel: (a) porosity; (b) permeability in the  $x$  east direction (PermX); and (c) permeability in the  $y$  north direction (PermY).

illumination as a function of various parameters such as survey geometry, overburden, burial depth and wavelet (Fig. 4).

A complete description of the technique is given in Lecomte (2008), and its direct application to 3D geological modelling of faults in Botter *et al.* (2016). The structural input to the PSDM simulator is an incident-angle-dependent reflectivity grid obtained from the elastic properties  $V_p$ ,  $V_s$  and  $\rho$  (Fig. 4a). In the wavenumber domain, ray-based modelling results are used to generate so-called PSDM filters, which are dependent on the survey geometry,

frequency content, wave type and velocity model (Fig. 4b). The reflectivity grid is converted to the wavenumber domain by a fast Fourier transform (FFT) and then multiplied by the PSDM filter. Applying an inverse FFT on this product gives the final simulated seismic image in the spatial domain (Fig. 4c). This process is equivalent to a 3D spatial convolution of the reflectivity grid with the inverse FFT of the PSDM filter (i.e. the point-spread function: PSF) (Fig. 4d). The PSF corresponds to the point-scatter response of the simulated PSDM process.

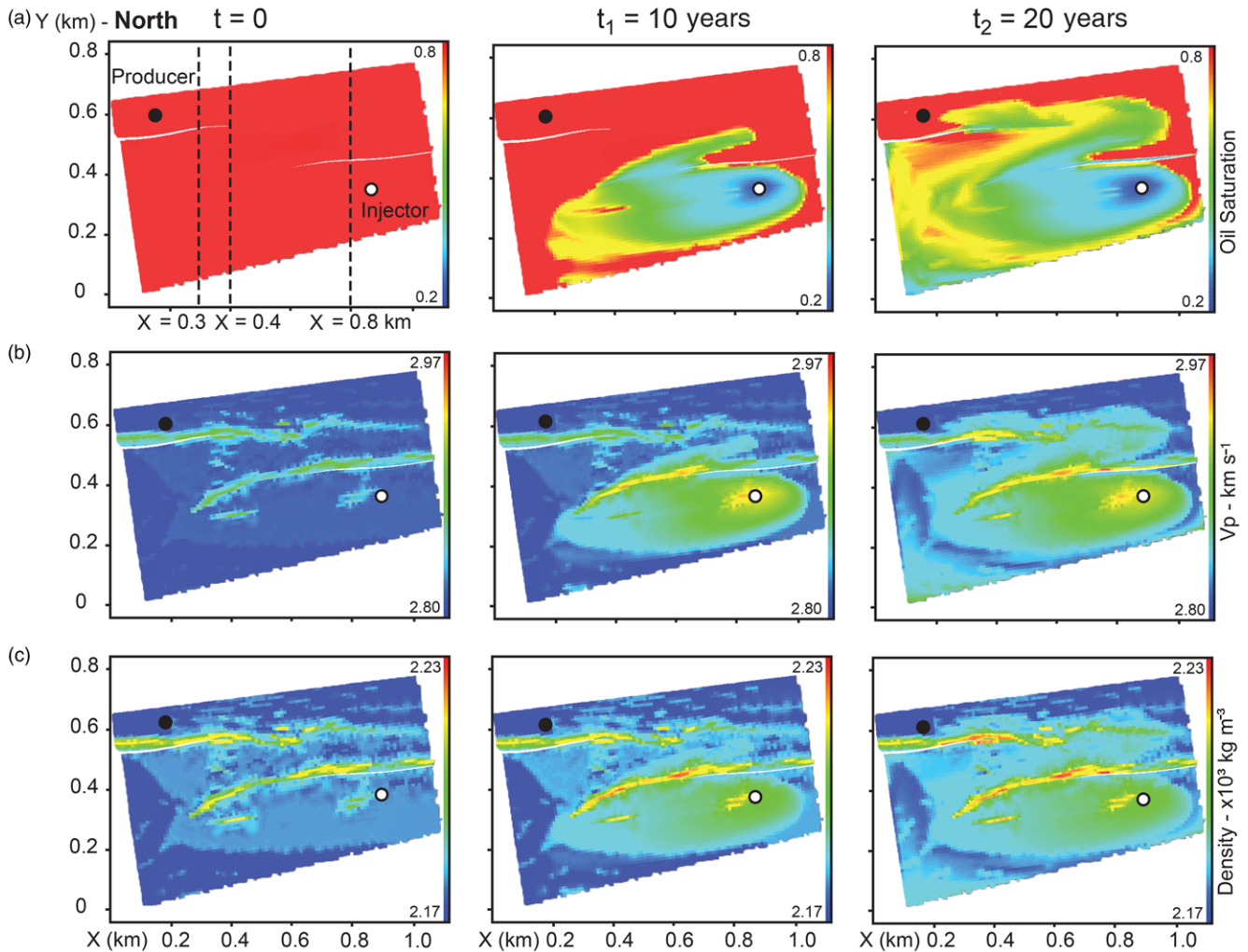


**Fig. 7.** Top view of the results at three stages of the fluid-flow simulation: (a) oil saturation; (b) P-wave velocity; and (c) density. The first column corresponds to  $t = 0$  when the reservoir is oil saturated, the second column to  $t_1 = 10$  years and the third column to  $t_2 = 20$  years. The injector (white circle) and the producer (black circle) wells are displayed in all of the images. The dashed lines in (a) are the lines of sections in Figures 9 and 10.

### Attribute-based seismic volume extraction

Once 3D seismic cubes are obtained, we can apply seismic-attribute-based automated techniques to extract the volume corresponding to the faults and related deformations. The chosen seismic attributes can be combined in order to better define the faults, the relay ramp or the fluid contacts. Iacopini & Butler (2011), Botter *et al.* (2016) and Iacopini *et al.* (2016) describe the seismic attributes for fault characterization and fault-damage volume extraction. Two seismic attributes are considered in this study: the tensor and the structurally orientated semblance attributes. The tensor attribute is based on a structurally orientated tensor, which is analysed to find the dominant dip direction of the reflectors and their 3D geometry (Gersztenkorn & Marfurt 1999). The semblance attribute looks for a similarity of traces within the seismic cube to identify abrupt mismatches in amplitude along the reflectors (Bahorich & Farmer 1995). The structurally orientated semblance algorithm can identify subtle structural and stratigraphic features that are not represented by peaks, troughs or zero crossings (Iacopini & Butler 2011; Iacopini *et al.* 2012, 2016). According to the stage of the flow simulation, we can apply either the tensor attribute alone (one-fluid model), or a combination of tensor and semblance attributes (water-invaded models).

The next step is the extraction of the faults or relay-ramp volume (depending on the fluid contacts). First, a fault-enhancement filter is applied to the attribute cubes to improve the continuity along faults. The size of this filter helps to define larger or smaller features on the attribute cube. This filter is only a support for the next fault detection filter that turns the potential faults into fault planes. The output volume shows the fault planes with an associated confidence factor. Starting from these fault planes, a fault-damage geobody is extracted by a growing process that adds new voxels to the geobody if they are connected to existing geobody voxels and are within a defined attribute threshold. We can then evaluate the extracted geobody qualitatively by displaying it back into the input data (i.e. seismic and property cubes).

## Results of seismic imaging

### Workflow parameters

Figure 5 shows the main variables tested in the workflow (Fig. 2). Each step of the methodology describes the parameters that are needed for the next step. We illustrate the workflow with a base case corresponding to reasonable geological settings and acquisition conditions (Fig. 5, parameters in bold). The base case was run first and then sensitivity analyses were applied to study the impact of rock properties and of seismic acquisition on seismic images. Only a few cases were presented, without analysing the impact of uncertainties in the parameter values, which is beyond the scope of the paper. In the geomodel, we focused on porosity and permeability for a given trend of deformation-band frequency. We first used the arithmetic average for the porosity (Equation 1) and then exaggerated the impact of deformation bands to produce lower porosity values. The permeability was first computed using the median value of deformation bands permeability (i.e.  $K_{DB} = 1$  mD) and later using a lower value of  $K_{DB} = 0.01$  mD (Rotevatn *et al.* 2009). We considered three stages of fluid-flow simulation: (1) at  $t = 0$  when the reservoir is oil saturated; (2) at  $t_1 = 10$  years when water starts to displace oil; and (3) at  $t_2 = 20$  years when water reaches the producer well. These three stages were used for seismic imaging and interpretation. The reflectivity grid (elastic parameters), the survey geometry (full-coverage survey), the overburden type (gradient) and the wave type (PP-wave) were constant in all simulations. To explore different geological and acquisition settings, we considered two cases for reservoir depth (2 or 1 km) and wave frequency (40 or 20 Hz). Seismic-attribute-based volume extraction was applied to all seismic images.

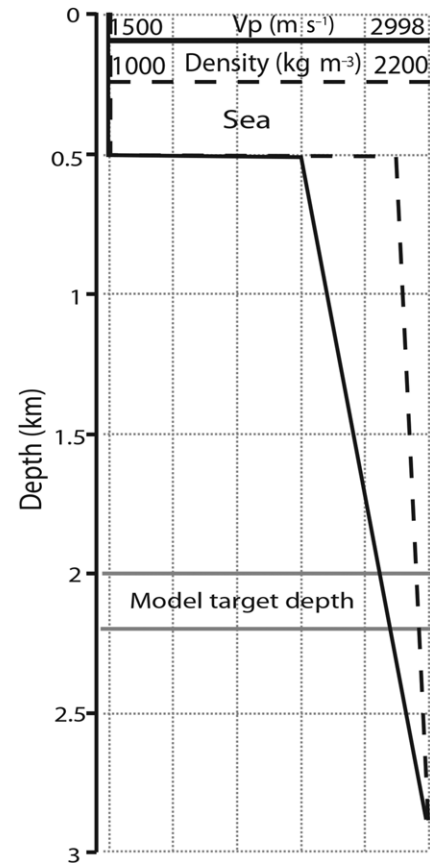


Fig. 8. Graph showing the increase in the elastic properties,  $V_p$  and density, in the overburden from a sea bottom at 500 m to the target depth of the model at 2000 m.

## Results and interpretation of the base case

### Rock properties

Using an arithmetic average with a deformation-band porosity of 1%, the computed porosity shows a maximum decrease of 11.4% of its initial value, with larger changes occurring in narrow zones along the two normal faults and ahead of their tiplines (Fig. 6a). A deformation-band permeability of 1 mD produces a decrease in the permeability of two orders of magnitude in the  $x$ -direction (Fig. 6b) and three orders of magnitude in the  $y$ -direction (Fig. 6c). Overall, the rock property changes follow the trends of the deformation band (Fig. 3c), but with greater changes for the permeability than for the porosity.

### Fluid-flow simulation and elastic properties

Using the base-case porosity and permeability (Fig. 6), we ran a flow simulation with parameters similar to those of Rotevatn *et al.* (2009) (Table 1). Figure 7a shows the location of the injector and producer wells, and the oil-saturation outputs at the three stages of the flow simulation. The first column corresponds to  $t = 0$  when the reservoir is 80% oil saturated. The second column is at  $t_1 = 10$  years when the waterfront has started to move up the relay ramp. The third column shows the simulation after 20 years when the waterfront has reached the producer well. Water invasion through the relay ramp is directly controlled by the permeability in both directions (Fig. 6b, c), which is influenced by the faults and the presence of deformation bands within the relay ramp (Fig. 3b, c).

Using Gassmann relationships, we computed the elastic properties ( $V_p$ ,  $V_s$  and  $\rho$ ) at the three stages of the fluid-flow simulation (Fig. 7b, c). When the model is oil saturated (Fig. 7b,



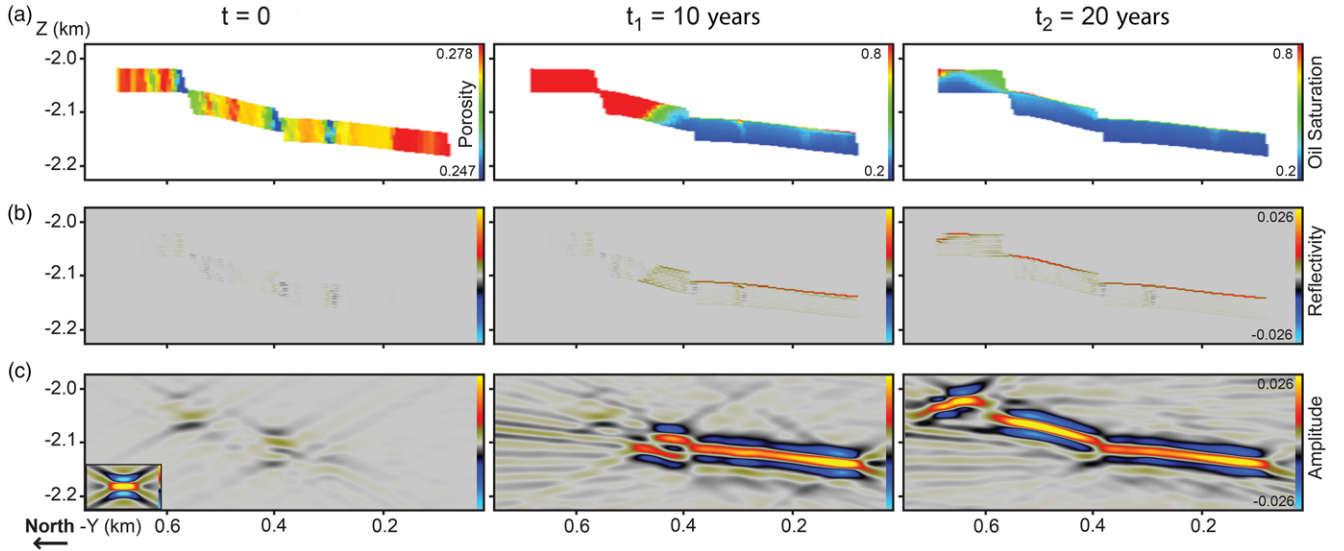


**Fig. 9.** Seismic section at  $x = 400$  m at the three stages of the flow simulation,  $t = 0$  (first column),  $t_1 = 10$  (second column) and  $t_2 = 20$  years (third column). (a) Porosity. (b) Reflectivity. (c) Seismic image with a 40 Hz Ricker pulse. The PSF in cross-sectional view is displayed on the bottom left-hand corner of (c) in the first column.

left), the velocities are directly related to the porosity grid (Fig. 6a).  $V_p$  increases where porosity decreases, with a maximum increase of 4% of its initial value. When the water invades the relay ramp, and both oil and water are present (Fig. 7b, middle and right),  $V_p$  follows both the porosity and the oil-saturation trends. The  $V_p$  value increases where water saturation increases. For a high degree of water saturation, the maximum increase in  $V_p$  is 7% of its initial value.  $\rho$  (Fig. 7c) shows similar behaviour, with a maximum increase of 2.8% of its initial value for the maximum porosity decrease (Fig. 7c, left), and 3.2% of its initial value for the maximum water saturation increase (Fig. 7c, middle and right). Water-saturation changes (up to 80%) have a stronger impact on the elastic properties than porosity changes of 11%. The elastic properties changes are even more important when the increase in water saturation is coupled to areas of low porosity (along the faults). We therefore expect seismic imaging of the relay ramp to be more dependent on the fluid contacts.

### Seismic images

The elastic properties are used to compute an incident-angle reflectivity grid, which is the input for the PSDM simulator. Several simulator parameters need to be defined in order to obtain seismic images at the conditions defined for the base case (Fig. 5). The

model was first brought to a depth of 2 km, which corresponds to the estimated depth of formation at the time of faulting (Rotevatn *et al.* 2007 and references therein). This depth corresponds to average velocities and density values of  $V_p = 2770$  m s<sup>-1</sup> and  $\rho = 2100$  kg m<sup>-3</sup> for high-porosity sandstone (Mavko *et al.* 2009). We defined an overburden with elastic properties linearly increasing from an assumed sea-bottom depth of 500 m (seawater:  $V_p = 1500$  m s<sup>-1</sup> and  $\rho = 1030$  kg m<sup>-3</sup>; Batzle & Wang 1992) to the targeted depth (Fig. 8). The marine survey was centred above the model, with 16 shot lines and six east-orientated (along the  $x$ -axis) streamers fully covering the model. We used a 40 Hz zero-phase Ricker pulse (Fig. 5), which gave us a vertical resolution of 17.5 m. The horizontal resolution can be estimated by looking at the PSFs in Figure 9, which is at its lowest 50 m in the north direction ( $y$ -axis). For all of the synthetic seismic cubes, the amplitude was calibrated such that a reflectivity of intensity 1 corresponds to an amplitude value of 1 on the seismic image.

Figure 9 shows the result of the PSDM simulation for the cross-line  $x = 400$  m indicated in Figure 7a, left. At  $t = 0$  (Fig. 9, left), the reflectivity is only slightly affected by the porosity trend. The corresponding seismic image at 40 Hz, however, has higher amplitude values than the reflectivity. We can therefore distinguish some reflection and diffraction at the two fault locations, but not the fault offset. The illuminated areas correspond to the reflectivity

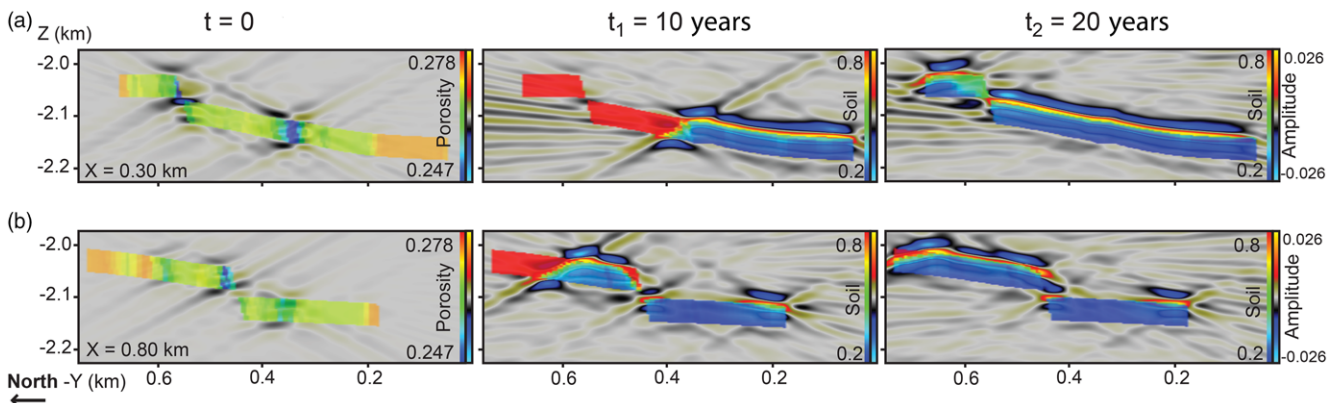


**Fig. 10.** Seismic sections at (a)  $x = 300$  m and (b)  $x = 800$  m, at the three stages of the flow simulation. The porosity is displayed with semi-transparency on top of the seismic section at  $t = 0$ , and the oil saturation is displayed on top of the seismic sections at  $t_1 = 10$  and  $t_2 = 20$  years.

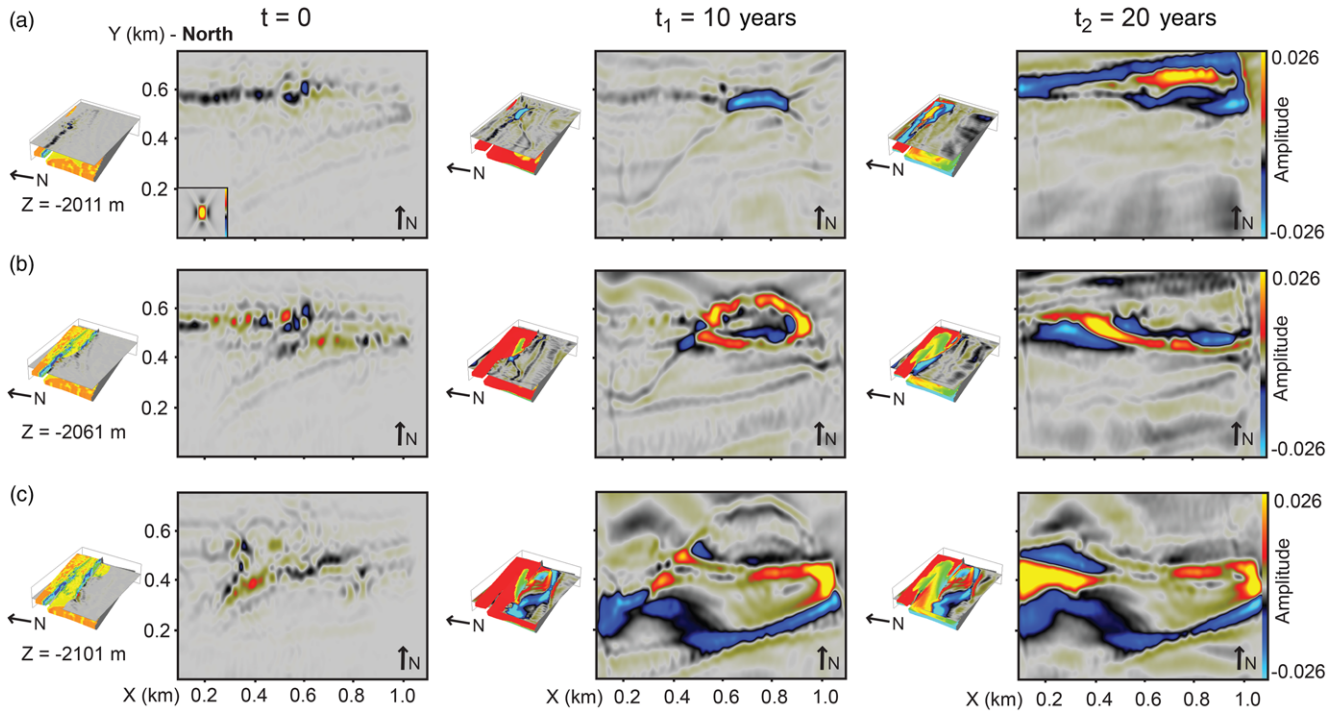


**Fig. 11.** Depth slices at elevation  $z$  equal to (a)  $-2011$  m, (b)  $-2061$  m and (c)  $-2101$  m for the three stages of the flow simulation (columns). Location of the depth slices is indicated in the 3D input properties cubes to the left of the slices: porosity for  $t=0$ ; and oil saturation for  $t_1=10$  and  $t_2=20$  years. The PSF in depth is displayed on the bottom left corner of a in the first column.

around the faults (i.e. the damage zone), but the discernible reflectivity area south of the southern fault is almost not visible on the seismic image. At  $t_1=10$  years (Fig. 9, middle), the oil–water contact has migrated up the reservoir, and is now located in the ramp and is almost coincident with the top of the lower part of the reservoir: hence, creating a reflective event. These fluid contacts have much a larger impact on the reflectivity than the porosity. Therefore, the northern fault with larger throw is not visible on the seismic image, whereas the southern fault is, owing to a break in the reflector of the thin oil layer at the top of the reservoir. At  $t_2=20$  years (Fig. 9, right), the water has invaded most of the relay ramp and the oil–water contact is coincident with the top of the entire relay ramp. This layer of high reflectivity is fully illuminated in the seismic image. The two faults are then indicated by a break in this reflector, the difference in their throws is visible, and the ramp is well defined between the faults, but the fault damage zones are not.

Figure 10 shows two additional seismic sections (indicated in Fig. 7a) at  $x=300$  m (Fig. 10a), where the section crosses only the northern fault, and at  $x=800$  m (Fig. 10b), where the section crosses only the southern fault. The two images at  $t=0$  confirm that the faults are imaged on the seismic profile because of their changes in porosity and not because of their offset (overlay transparency in Fig. 10, left; Fig. 3b). The  $x=300$  m section displays strong reflections corresponding to the damage zone of the southern fault to the west where there is no fault offset; in the  $x=800$  m section, however, the reflections are lower around the southern fault itself, owing to its smaller changes in porosity. At  $t_1=10$  years, the fluid contacts (overlay transparency in Fig. 10, middle) show the influence of the low-porosity area west of the southern fault on the  $x=300$  m section. This low-porosity area effectively stops the water front (Fig. 10a, middle). The oil–water contact also highlights the presence of the southern fault on the  $x=800$  m section (Fig. 10b, middle). The offset of the fluid contacts at  $t_2=20$  years (overlay transparency in Fig. 10, right) marks the northern and southern faults. However, identifying the faults from the fluid contacts alone could be difficult, especially when these contacts change laterally, as in the area close to the injector well.

Depth slices help to better define the faults and the relay ramp. Figure 11 presents depth slices at three elevations for the three stages of the flow simulation. The three seismic slices at  $t=0$  when the model is oil saturated (Fig. 11, left) define the two faults and the relay ramp, even where the separation distance between the two faults is the smallest. At  $t_1=10$  years (Fig. 11, middle), the strong reflections controlled by the fluid contacts allow the extent of water invasion in the relay ramp to be delimited. The northern fault is visible on the upper section and the southern fault can be interpreted by the linear trend of strong reflections of the waterfront. After water breakout at  $t_2=20$  years (Fig. 11, right), the entire water body is determined by strong reflectors. The three depth slices allow the relay ramp and the two faults to be interpreted by studying the displacement of water.

#### Attribute-based volume extraction

Using the methodology described in the earlier subsection on ‘Attribute-based seismic volume extraction’, we extracted the fault volumes (fault-damage zones) from the seismic cubes at the three stages of the flow simulation (Fig. 12). The seismic attributes were adapted for each model. At  $t=0$ , when the reservoir is oil-saturated, the best way to define the faults is to use only the tensor attribute. Based on this tensor cube, a fault geobody was extracted applying the fault-enhancement and fault-detection filters (Fig. 12a, left). This geobody represents the most probable fault volume based on the visible expression of the fault in the seismic cube and the subsequent attribute volume. To better appreciate the accuracy of the geobody, we displayed it back in the porosity cube (Fig. 12b, left). The extracted geobody captures the two faults and their damage zones as independent entities and, to some extent, suggests the presence of the relay ramp, even if it displays linkage of the two faults in the most eastern part of the ramp. The geobody is limited by the boundaries of the attribute cubes on the eastern side of the model.

At  $t_1=10$  and  $t_2=20$  years, a combination of the tensor and semblance attributes helps to better define the faults and the fluid contacts from the extracted volumes (Fig. 12, middle and right). The



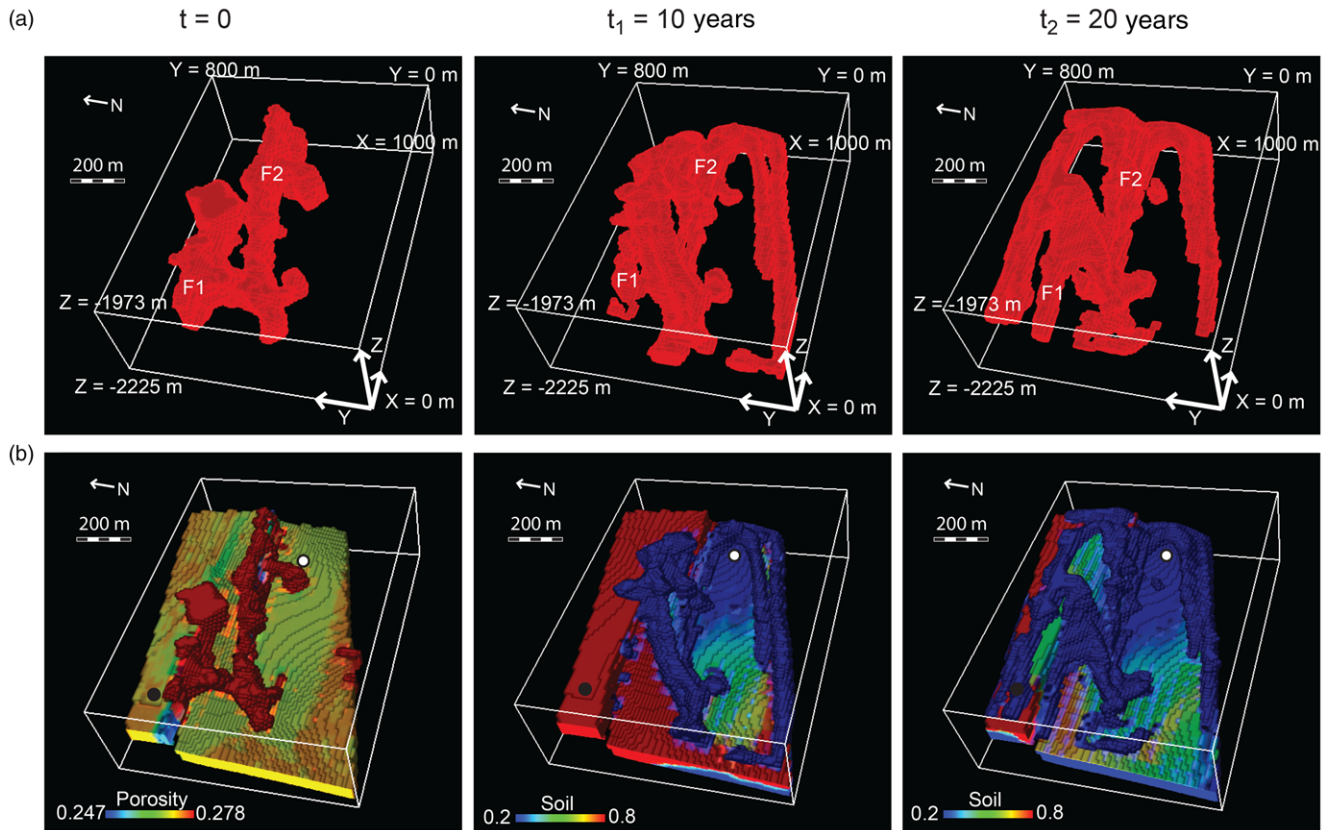


**Fig. 12.** (a) Extracted geobody volumes at the three stages of the flow simulation (columns) and (b) geobody volumes displayed back in the porosity cube for the model at  $t = 0$  (geobody in red), and the oil saturation cubes for the models at  $t_1 = 10$  and  $t_2 = 20$  years (geobody in blue). F1 and F2 indicate the locations of the two normal faults. The location of the injector (white circle) and producer (black circle) wells are indicated in (b).

fault-enhancement, with a smaller filter size than for the first model, and detection filters are applied to this combined seismic attribute cube. At  $t_1 = 10$  years, the extracted volume delimits mainly the water body, including the water moving through the relay ramp, which can be used to define the extent of this structure (Fig. 12, middle). Patches of the northern fault are also extracted in its most eastern part. At  $t_2 = 20$  years, the water body extends from the lower part of the relay ramp (i.e. around the injector well) to the upper part (i.e. the producer well) (Fig. 12, right). The southern and northern faults are well marked, with a clear zone connecting them shown by the water that has invaded the relay ramp. Thus, we are able to define the two faults and their permeability barriers at the three stages of the fluid-flow simulation. At  $t_1 = 10$  and  $t_2 = 20$  years, we are also able to delimit the relay ramp by extracting the water bodies.

#### Impact of workflow parameters

We vary some of the workflow parameters (Fig. 5) in order to consider different geological settings or seismic acquisition conditions.

#### Impact of wave frequency

The frequency content of the wavelet is easily manipulated in the PSDM simulator. A lower dominant frequency of 20 Hz can be more realistic at a depth of 2 km. Figure 13c shows the impact of this lower frequency for the same seismic section as in Figure 9 ( $x = 400$  m) at the three stages of fluid-flow simulation. These new sections have lower vertical and horizontal resolutions than the base case at 40 Hz (Fig. 13b), but the two fault locations are still visible at  $t = 0$  (Fig. 13c, left). The faults, however, are not well imaged on the later-stage models (Fig. 13c middle and right). Only the northern fault can be interpreted at  $t_2 = 20$  years. The oil–water contact at  $t_1 =$

10 years, which can be observed on the 40 Hz seismic image (Fig. 13b), is not observed on the 20 Hz seismic image (Fig. 13c).

#### Impact of depth

Changing the overburden depth of the model to a shallower depth could better highlight the porosity detail over the fluid contacts, as it would decrease the damping impact of the overburden and increase the resolution. Keeping the base workflow parameters and including the gradients of elastic properties with depth (Fig. 8), we place the model at a lower depth of 1 km. The reflectivity is not very different to the base case (Fig. 13a), although it has slightly stronger values. The results for the same seismic section are shown in Figure 13d. First, much more diffraction is visible at 1 km (Fig. 13d) than at 2 km depth (Fig. 13b). The resolution is higher and more detail is visible, especially the reflectivity (and porosity) changes on the  $t_1 = 10$  and  $t_2 = 20$  years models (Fig. 13d, middle and right). The seismic images for the shallow reservoir are more complex and, perhaps, more difficult to analyse, although they make the changes in rock properties as a result of fault damage easier to identify.

#### Impact of rock properties

We can modify the values of porosity and permeability of the reservoir model and keep the same PSDM simulator parameters as the base case. A maximum decrease of 50% in the initial porosity due to the deformation bands is, perhaps, unrealistic but it would truly highlight the fault-damage zones (Fig. 14a, left). In addition, we can assign the deformation bands a low permeability of 0.01 mD, this results in a stronger influence of the deformation bands on the fluid flow. These two changes impact the flow simulation, resulting in a longer running time (55 years) and in bypassed areas with large concentrations of deformation bands

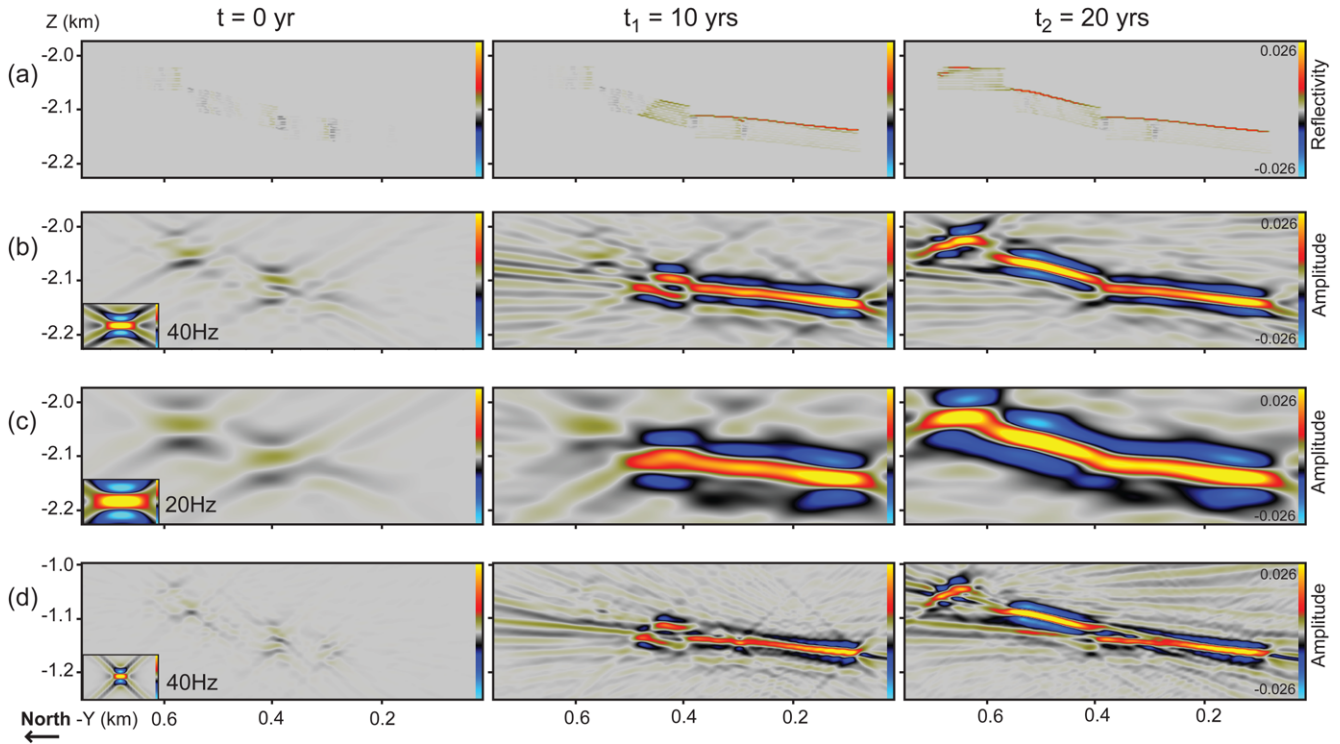


**Fig. 13.** Seismic section at  $x = 400$  m to evaluate the impact of PSDM simulator parameters on seismic images at the three stages of the fluid-flow simulation (columns). (a) Reflectivity of the base case; (b) seismic images corresponding to base case with a 40 Hz Ricker pulse; (c) seismic images corresponding to the base case with a 20 Hz Ricker pulse; and (d) seismic images at 1 km depth with other parameters corresponding to the base case and 40 Hz Ricker pulse. The PSFs in cross-sectional view are displayed in the bottom left-hand corner of each seismic image in the first column.

(Fig. 14a, middle and right). The corresponding reflectivity grids show as much intensity for the change in porosity values (Fig. 14b, left) as for the fluid contacts (Fig. 14b, middle and right). These effects are clearly observable on the seismic images (Fig. 14c). At  $t = 0$ , the fault zones can be identified (Fig. 14c, left) as opposed to the base case where they are subtle (Fig. 13b, left). When oil and water are present in the relay ramp, at  $t_1 = 30$  and  $t_2 = 55$  years, it is still possible to identify the two faults as separate structures, even though the water has invaded the relay ramp (Fig. 14c, middle and right).

### Discussion and conclusions

The workflow of Figure 2 has been designed to study the impact of faults, fault-related deformation and fluid contacts during production on seismic images of a soft-linked relay ramp. Our main objective was to study the response of a relay ramp structure and its fluid composition on seismic images acquired during reservoir production, and to improve their characterization and interpretation.

The Delicate Arch Ramp is a well-exposed, seismic-scale outcrop analogue of a relay ramp, with a well-mapped distribution of rock

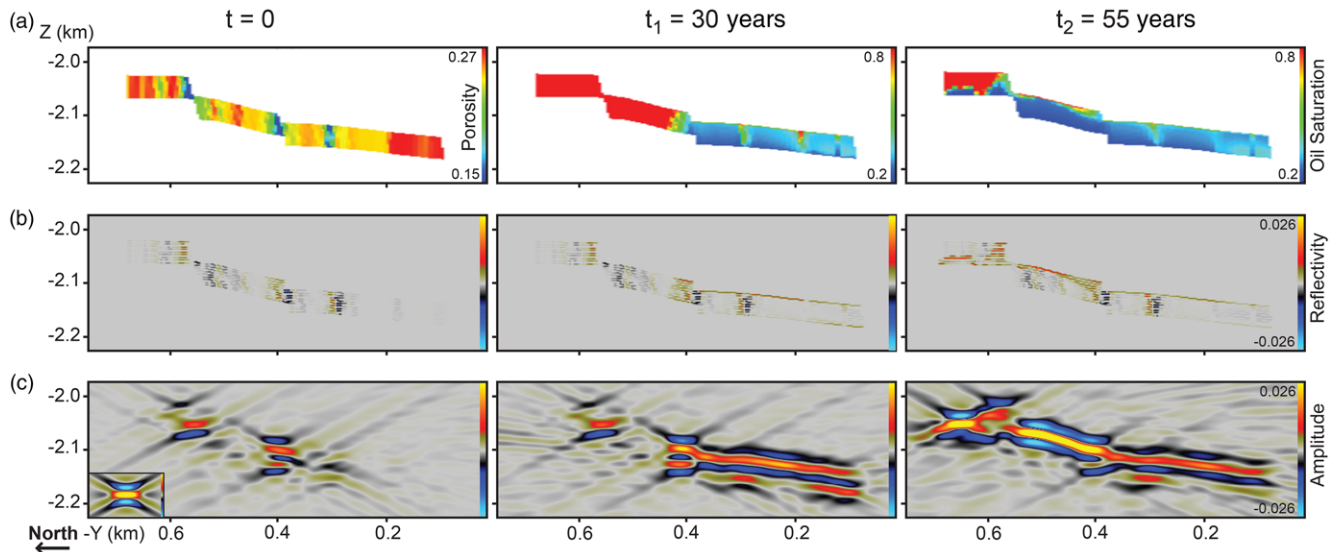


**Fig. 14.** Seismic section at  $x = 400$  m for the modified rock properties of Figure 5 and at the three stages of the flow simulation:  $t = 0$  (first column),  $t_1 = 30$  years (second column) and  $t_2 = 55$  years (third column). The input properties (i.e. porosity at  $t = 0$ , and oil saturation at  $t_1 = 10$  and  $t_2 = 20$  years) are shown in (a), the corresponding reflectivity in (b) and the seismic images with a 40 Hz Ricker pulse in (c). The PSF in cross-sectional view is displayed in the bottom left-hand corner of (c) in the first column.

properties (Rotevatn *et al.* 2007). This outcrop analogue has been the basis of several reservoir modelling studies (e.g. Rotevatn *et al.* 2009; Rotevatn & Fossen 2011; Fachri *et al.* 2013). Modelling a homogeneous, relatively clean sandstone reservoir allows us to focus on the seismic response of fault damage rather than on the impact of facies changes because of depositional processes or fault offsets. From the initial high-porosity Entrada sandstone, we have good control over the impact of deformation bands on porosity and permeability. Even if the outcrop model is specific, the reservoir modelling was performed using a range of variable damage-zone properties, where deformation-band frequency and permeability were varied between the different simulations (Rotevatn *et al.* 2009), expanding the range of applications. Even if the faults in the geomodel are defined as surfaces, their damage zones (zones of high deformation-band frequency) give them a three-dimensionality that can be investigated in the seismic images. The changes in porosity due to the deformation bands in the relay ramp have low relative seismic amplitude variations that are not visible in the two-fluid models during production. Yet, they still impact the initial, oil-saturated seismic images, mainly because of deformation-band frequency (an expression of fault damage) and not fault throw. However, if the model were part of a more heterogeneous reservoir, or if the deformation bands had a lower impact on rock properties, there would be some additional sedimentological, stratigraphical and fault juxtaposition effects influencing the fault-damage zone seismic response. The results of this study should be extrapolated with care to other situations involving other type of reservoirs, and other type of mesoscopic structures resulting from fault damage.

The thickness of the model is one of the main limitations of our reservoir model. Arguably, it may or may not be useful to investigate further into the topic of seismic imaging of this thin-bedded reservoir layer. It is possible that if this thin-bedded unit were incorporated into a geological sequence, fewer details would be discernible on the seismic data. The results of the section on 'Results of seismic imaging' show that in a homogeneous, but faulted, sandstone layer there is very little information visible on the seismic data. The changes in rock properties caused by the deformation bands are almost impossible to identify during production and fluid displacement, although they influence the seismic image. Helped by an appropriate tuning of the seismic-attribute analysis (Chopra & Marfurt 2005; Botter *et al.* 2016), we are able to extract damage areas around the faults, even if the fluid contacts have a much stronger impact (Fig. 12). As the water invades the relay ramp, the extracted geobody captures more of the water body than the faults. The outcome of seismic-attribute analysis helps to better define the soft-linked relay ramp as a conduit for fluid flow as production progresses (Fig. 12). Our seismic-attribute study is complementary to those of Dutzer *et al.* (2010), Iacopini & Butler (2011) and Iacopini *et al.* (2016) on real datasets, and to Botter *et al.* (2016) on synthetic seismic data. These studies highlight that the attribute interpretation workflow is very much dependent on the quality of the input data. Seismic attributes can enhance subtle noise, therefore, to expand the application of this visualization workflow to real datasets; one needs to be familiar with the acquisition and processing steps applied to the seismic data and with the assumptions behind the attributes in order to avoid pitfalls in the structural interpretation (Marfurt & Alves 2015). Additional quantitative analyses of the extracted geobodies can be conducted to investigate the correlation between seismic amplitudes, seismic facies and, potentially, rock properties relying on a rock physics model (Botter *et al.* 2016). The fine grid of our reservoir model is likely to be impractical for modelling a large-scale producing oil field, but it is crucial for the accurate representation of the relay-ramp structure and petrophysical properties, simulating flow tortuosity. The small details are indeed handled by PSDM simulator and upscaled to seismic scale. The

results of the workflow are therefore dependent on the resolution of the input reservoir model.

Despite the specific input of our workflow (i.e. the Delicate Arch reservoir model), many other parameters can be varied in order to run sensitivity analyses or to target real reservoir conditions. Rotevatn *et al.* (2009) explored a large range of deformation-band frequencies and permeability values for the fluid-flow simulation. In this paper, we illustrate the workflow with only one set of parameters for fluid flow (Table 1), but more combinations can be tested. We have presented two end cases for porosity and permeability values. A stronger impact of the deformation bands on porosity and permeability results in stronger reflectivity fields before production, and better imaging of the faults throughout production (Fig. 14). This high impact of deformation bands on rock properties is, perhaps, unrealistic for sandstone, but it might be appropriate for other lithologies and structures. One of the strong advantages of the workflow is the possibility of quickly and efficiently exploring reservoir and acquisitions conditions. Several parameters, such as wave frequency, overburden and reservoir depth, are crucial. The faults and the relay ramp are better defined on seismic images at shallower depths (Fig. 13d) and higher wave frequencies (Fig. 13b, c). Other geological parameters can negatively affect the seismic response of the relay ramp, such as a more complex overburden, overpressures and greater depths. These observations are also relevant for thicker sedimentary sequences, larger geological structures and more complex production scenarios.

Our workflow establishes a link between geology, geophysics and reservoir modelling. By using an outcrop-based model as input, we have control over the geometry of the relay ramp, fault damage zones and petrophysical properties. By putting the model under production conditions and running seismic modelling, it helps the geologist to evaluate the seismic response of the relay ramp and its relationship to fluid flow. Fault sealing during production is dynamic (Yielding *et al.* 2010). When water is invading an oil-saturated reservoir, the extracted water body enables the interpretation of the relay ramp and an overview of permeability barriers. 4D seismic imaging during production can add further constraints to the interpretation, even at the limit of seismic resolution. This workflow helps the geophysicist to acquire and process seismic data with a better geological knowledge, and with the objective of illuminating faults and fluids. Naturally, the workflow integrates the reservoir engineer by linking fluid flow in the reservoir model to the seismic images. Finally, our methodology can also help to constrain seismic inversion techniques by using parameter values from seismic inversion in this workflow and comparing the modelled seismic images with the seismic data. Future work will apply these techniques to seismic and production data.

## Acknowledgements and Funding

This work was funded by the Norwegian Research Council through the project 'Seismic Imaging of Fault Zones' (NFR-PETROMAKS, project No. 210425/E30). The geomodel of the Delicate Arch Ramp was constructed by Atle Rotevatn using RMS (Emerson–Roxar). The fluid-flow simulation was run in Eclipse (Schlumberger), seismic imaging simulation was performed in SeisRoX (NORSAR), and seismic attributes analysis was performed using SVI plus (GeoTeric) and a fault-damage mapping toolkit developed by GeoTeric. We thank Hans Kleppe at the University of Stavanger for his help with the fluid-flow simulation. The reviewers and the editors are thanked for their insight and constructive feedback, which helped to improve the manuscript.

## References

- Antonellini, M. & Aydin, A. 1994. Effect of faulting on fluid flow in porous sandstones: petrophysical properties. *American Association of Petroleum Geologists Bulletin*, **78**, 355–377.
- Antonellini, M. & Aydin, A. 1995. Effect of faulting on fluid flow in porous sandstones: geometry and spatial distribution. *American Association of Petroleum Geologists Bulletin*, **79**, 642–671.
- Bahorich, M. & Farmer, S. 1995. 3-D seismic discontinuity for faults and stratigraphic features: The coherence cube. *The Leading Edge*, **14**, 1053–1058.



- Batzle, M. & Wang, Z. 1992. Seismic properties of pore fluids. *Geophysics*, **57**, 1396–1408.
- Botter, C., Cardozo, N., Hardy, S., Lecomte, I., Paton, G. & Escalona, A. 2016. Seismic characterisation of fault damage in 3D using mechanical and seismic modelling. *Marine and Petroleum Geology*, **77**, 973–990.
- Childs, C., Watterson, J. & Walsh, J.J. 1995. Fault overlap zones within developing normal fault systems. *Journal of the Geological Society, London*, **152**, 535–549, <http://doi.org/10.1144/gsjgs.152.3.0535>
- Chopra, S. & Marfurt, K.J. 2005. Seismic attributes – a historical perspective. *Geophysics*, **70**, 3SO–28SO.
- Doelling, H.H. 2001. *Geologic Map of the Moab and Eastern Part of the San Rafael Desert 30' 60' Quadrangles, Grand and Emery Counties, Utah, and Mesa County, Colorado. Map 180*. Utah Geological Survey, Salt Lake City, UT, USA.
- Dutser, J.F., Basford, H. & Purves, S. 2010. Investigating fault-sealing potential through fault relative seismic volume analysis. *Petroleum Geology Conference Proceedings*, **7**, 509–515.
- Fachri, M., Rotevatn, A. & Tveranger, J. 2013. Fluid flow in relay zones revisited: Towards an improved representation of small-scale structural heterogeneities in flow models. *Marine and Petroleum Geology*, **46**, 144–164.
- Fossen, H. & Bale, A. 2007. Deformation bands and their influence on fluid flow. *American Association of Petroleum Geologists Bulletin*, **91**, 1685–1700.
- Fossen, H. & Rotevatn, A. 2016. Fault linkage and relay structures in extensional settings – A review. *Earth-Science Reviews*, **154**, 14–28.
- Fossen, H., Schultz, R.A., Shipton, Z.K. & Mair, K. 2007. Deformation bands in sandstone: A review. *Journal of the Geological Society, London*, **164**, 755–769, <http://doi.org/10.1144/0016-76492006-036>
- Gassmann, F. 1951. Elasticity of porous media. *Vierteljahrsschr der Naturforschenden Gessellschaft*, **96**, 1–23.
- Gersztenkorn, A. & Marfurt, K.J. 1999. Eigenstructure-based coherence computations as an aid to 3-D structural and stratigraphic mapping. *Geophysics*, **64**, 1468–1479.
- Giba, M., Walsh, J.J. & Nicol, A. 2012. Segmentation and growth of an obliquely reactivated normal fault. *Journal of Structural Geology*, **39**, 253–267.
- Hesthammer, J. & Fossen, H. 1997. Seismic attribute analysis in structural interpretation of the Gullfaks Field, northern North Sea. *Petroleum Geoscience*, **3**, 3–26, <http://doi.org/10.1144/petgeo.3.1.1>
- Iacopini, D. & Butler, R.W.H. 2011. Imaging deformation in submarine thrust belts using seismic attributes. *Earth and Planetary Science Letters*, **302**, 414–422.
- Iacopini, D., Butler, R. & Purves, S. 2012. Seismic imaging of thrust faults and structural damage: a visualization workflow for deepwater thrust belts. *First Break*, **30**, 77–84.
- Iacopini, D., Butler, R.W.H., Purves, S., McArdle, N. & De Freslon, N. 2016. Exploring the seismic expression of fault zones in 3D seismic volumes. *Journal of Structural Geology*, **89**, 54–73.
- Kim, Y.-S., Peacock, D.C. & Sanderson, D.J. 2004. Fault damage zones. *Journal of Structural Geology*, **26**, 503–517.
- Lecomte, I. 2008. Resolution and illumination analyses in PSDM: A ray-based approach. *The Leading Edge*, **27**, 650–663.
- Lecomte, I., Lavadera, P.L., Anell, I., Buckley, S.J., Schmid, D.W. & Heeremans, M. 2015. Ray-based seismic modeling of geologic models: Understanding and analyzing seismic images efficiently. *Interpretation*, **3**, SAC71–SAC89.
- Lecomte, I., Lavadera, P.L. *et al.* 2016. 2(3)D convolution modelling of complex geological targets beyond – 1D convolution. *First Break*, **34**, 99–107.
- Long, J.J. & Imber, J. 2010. Geometrically coherent continuous deformation in the volume surrounding a seismically imaged normal fault-array. *Journal of Structural Geology*, **32**, 222–234.
- Long, J.J. & Imber, J. 2012. Strain compatibility and fault linkage in relay zones on normal faults. *Journal of Structural Geology*, **36**, 16–26.
- Manzocchi, T., Childs, C. & Walsh, J.J. 2010. Faults and fault properties in hydrocarbon flow models. *Geofluids*, **10**, 94–113.
- Marfurt, K.J. & Alves, T.M. 2015. Pitfalls and limitations in seismic attribute interpretation of tectonic features. *Interpretation*, **3**, SB5–SB15.
- Mavko, G., Mukerji, T. & Dvorkin, J. 2009. *The Rock Physics Handbook: Tools for Seismic Analysis in Porous Media* (2nd edn). Cambridge University Press, New York.
- Peacock, D.C.P. & Sanderson, D.J. 1994. Geometry and development of relay ramps in normal fault systems. *American Association of Petroleum Geologists Bulletin*, **78**, 147–165.
- Rotevatn, A. & Fossen, H. 2011. Simulating the effect of subseismic fault tails and process zones in a siliciclastic reservoir analogue: Implications for aquifer support and trap definition. *Marine and Petroleum Geology*, **28**, 1648–e1662.
- Rotevatn, A., Fossen, H., Hesthammer, J., Aas, T.E. & Howell, J.A. 2007. Are relay ramps conduits for fluid flow? Structural analysis of a relay ramp in Arches National Park, Utah. In: Lonergan, L., Sanderson, D.J., Jolly, R.J.H. & Rawnsley, K. (eds) *Fractured Reservoirs*. Geological Society, London, Special Publications, **270**, 55–71, <http://doi.org/10.1144/GSL.SP.2007.270.01.04>
- Rotevatn, A., Tveranger, J., Howell, J.A. & Fossen, H. 2009. Dynamic investigation of the effect of a relay ramp on simulated fluid flow: geocellular modelling of the Delicate Arch Ramp, Utah. *Petroleum Geoscience*, **15**, 45–58, <http://doi.org/10.1144/1354-079309-779>
- Torabi, A., Alaei, B. & Kolyukhin, D. 2016a. Analysis of fault scaling relations using fault seismic attributes. *Geophysical Prospecting*, <http://doi.org/10.1111/1365-2478.12440>
- Torabi, A., Alaei, B., Kolyukhin, D., Libak, R.H., Gabrielsen, R.H. & Braathen, A. 2016b. Fault geometric and seismic attributes – an integrated study with focus on the Barents Sea. *First Break*, **34**, 73–80.
- Walsh, J., Bailey, W., Childs, C., Nicol, A. & Bonson, C. 2003. Formation of segmented normal faults: a 3-D perspective. *Journal of Structural Geology*, **25**, 1251–1262.
- Yielding, G., Bretan, P. & Freeman, B. 2010. Fault seal calibration: a brief review. In: Jolley, S.J., Fisher, Q.J., Ainsworth, R.B., Vrolijk, P.J. & Delisle, S. (eds) *Reservoir Compartmentalization*. Geological Society of London, Special Publications, **347**, 243–255, <http://doi.org/10.1144/SP347.14>